Artificial Compressibility Solution of the Lid-Driven Cavity Problem

Rithwik Shankar Raj

1 Introduction

The lid-driven cavity problem is a canonical benchmark for validating numerical methods for incompressible viscous flow. In this configuration, a square cavity is enclosed by stationary walls on the left, right, and bottom boundaries, while the top wall moves with a constant tangential velocity. The moving lid induces a recirculating flow inside the cavity, producing a primary vortex in the interior and, at higher Reynolds numbers, increasingly pronounced corner vortices and sharper boundary layers.

In the present work, the cavity flow is solved using the artificial compressibility method on a staggered grid. Pressure and velocity are coupled by introducing a pseudo-time pressure evolution equation. The resulting formulation is iterated until a divergence-free steady state is obtained.

2 Problem Definition

A square cavity of side length $L = H = 1$ is considered. The top lid moves with unit horizontal velocity,

$$U_{\text{lid}} = 1,$$

while all other walls satisfy the no-slip condition. Two Reynolds numbers are studied:

$$Re = 100, \qquad Re = 400.$$

The Reynolds number is defined as

$$Re = \frac{\rho U_{\text{lid}} L}{\mu}.$$

Table 1 summarizes the principal problem parameters.

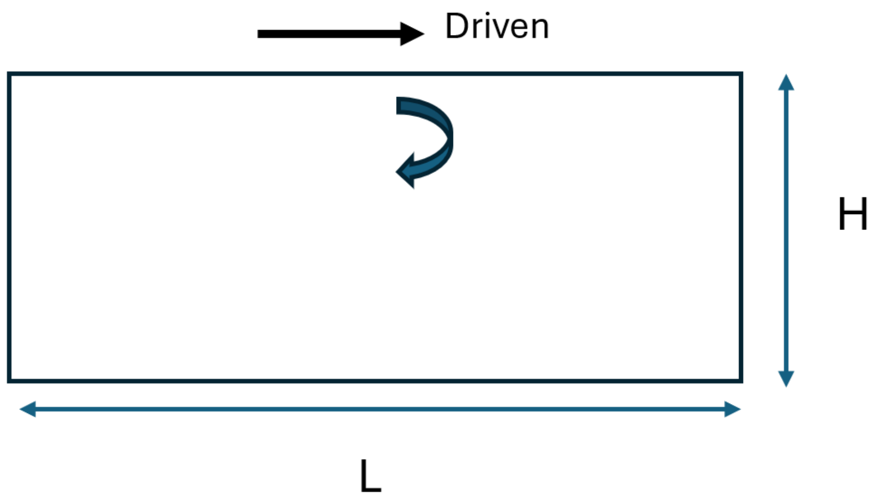

Figure 1: Schematic of the computational domain.

Table 1: Simulation parameters for the lid-driven cavity problem.

Quantity	Value
Cavity length, L	1
Cavity height, H	1
Lid velocity, U_{lid}	1
Reynolds numbers considered	100, 400
Artificial compressibility parameter, β	0.5
Continuity-residual tolerance	10^{-4}

3 Governing Equations and Artificial Compressibility Formulation

3.1 Incompressible governing equations

For an incompressible two-dimensional flow, the continuity equation is

$$\frac{\partial u}{\partial x} + \frac{\partial v}{\partial y} = 0, \tag{1}$$

and the momentum equations are

$$\frac{\partial u}{\partial t} + \frac{\partial (u^2)}{\partial x} + \frac{\partial (uv)}{\partial y} = -\frac{\partial p}{\partial x} + \frac{1}{Re}\left(\frac{\partial^2 u}{\partial x^2} + \frac{\partial^2 u}{\partial y^2}\right), \tag{2}$$

$$\frac{\partial v}{\partial t} + \frac{\partial (uv)}{\partial x} + \frac{\partial (v^2)}{\partial y} = -\frac{\partial p}{\partial y} + \frac{1}{Re}\left(\frac{\partial^2 v}{\partial x^2} + \frac{\partial^2 v}{\partial y^2}\right). \tag{3}$$

3.2 Artificial compressibility method

The artificial compressibility method replaces the incompressibility constraint with a pseudo-time pressure evolution equation,

$$\frac{1}{\beta}\frac{\partial p}{\partial \tau} + \frac{\partial u}{\partial x} + \frac{\partial v}{\partial y} = 0, \tag{4}$$

where τ is a pseudo-time and β is the artificial compressibility constant. At steady state in pseudo-time,

$$\frac{\partial p}{\partial \tau} = 0,$$

so Eq. (4) reduces exactly to the incompressible continuity equation in Eq. (1).

The corresponding pseudo-compressible system may be written in vector form as

$$\frac{\partial \mathbf{U}}{\partial \tau} + \frac{\partial \mathbf{E}}{\partial x} + \frac{\partial \mathbf{F}}{\partial y} = \frac{1}{Re}\left(\frac{\partial^2}{\partial x^2} + \frac{\partial^2}{\partial y^2}\right)\begin{bmatrix} 0 \\ u \\ v \end{bmatrix}, \tag{5}$$

with

$$\mathbf{U} = \begin{bmatrix} p/\beta \\ u \\ v \end{bmatrix}, \qquad \mathbf{E} = \begin{bmatrix} u \\ u^2 + p \\ uv \end{bmatrix}, \qquad \mathbf{F} = \begin{bmatrix} v \\ uv \\ v^2 + p \end{bmatrix}. \tag{6}$$

3.3 Explicit pseudo-time update

In compact form, the update can be written as

$$\Delta \mathbf{U} = \Delta\tau \left[-\frac{\partial \mathbf{E}}{\partial x} - \frac{\partial \mathbf{F}}{\partial y} + \frac{1}{Re}\left(\frac{\partial^2}{\partial x^2} + \frac{\partial^2}{\partial y^2}\right)\begin{bmatrix} 0 \\ u \\ v \end{bmatrix}\right]^n, \tag{7}$$

followed by

$$\mathbf{U}^{n+1} = \mathbf{U}^n + \Delta \mathbf{U}. \tag{8}$$

4 Spatial Discretization on a Staggered Grid

A staggered grid is used to avoid pressure–velocity decoupling: pressure is stored at cell centers, the horizontal velocity u is stored at vertical cell faces, and the vertical velocity v is stored at horizontal cell faces. This is the standard MAC-type arrangement used for incompressible flow solvers.

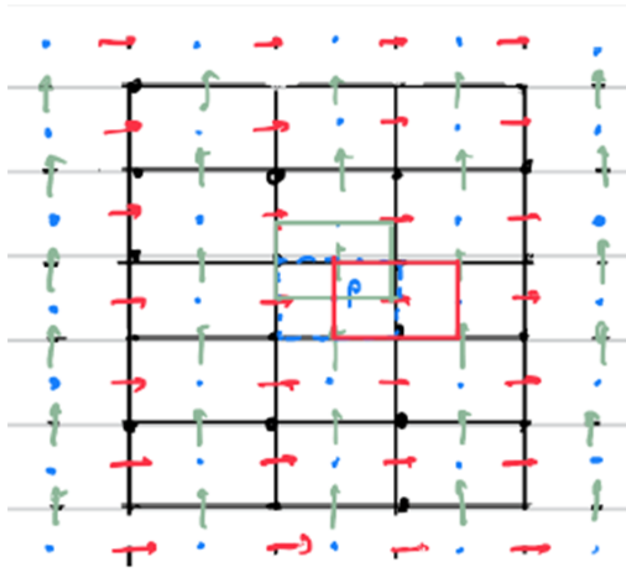

Figure 2: Schematic of the 2D staggered grid.

4.1 Discrete continuity equation

At a pressure control volume (i, j), Eq. (4) is discretized as

$$\frac{1}{\beta}\frac{p_{i,j}^{n+1} - p_{i,j}^{n}}{\Delta\tau} + \frac{u_{i,j}^{n} - u_{i-1,j}^{n}}{\Delta x} + \frac{v_{i,j}^{n} - v_{i,j-1}^{n}}{\Delta y} = 0. \tag{9}$$

Rearranging gives the explicit pressure update,

$$p_{i,j}^{n+1} = p_{i,j}^{n} - \beta\Delta\tau\left[\frac{u_{i,j}^{n} - u_{i-1,j}^{n}}{\Delta x} + \frac{v_{i,j}^{n} - v_{i,j-1}^{n}}{\Delta y}\right]. \tag{10}$$

4.2 Discrete x-momentum equation

For the horizontal velocity component, Eq. (2) is discretized explicitly as

$$\frac{u_{i,j}^{n+1} - u_{i,j}^{n}}{\Delta\tau} + \left(\frac{\partial u^2}{\partial x}\right)_{i,j}^{n} + \left(\frac{\partial uv}{\partial y}\right)_{i,j}^{n} = -\left(\frac{\partial p}{\partial x}\right)_{i,j}^{n} + \frac{1}{Re}\left[\left(\frac{\partial^2 u}{\partial x^2}\right)_{i,j}^{n} + \left(\frac{\partial^2 u}{\partial y^2}\right)_{i,j}^{n}\right]. \tag{11}$$

Using second-order central differences on the staggered grid, the convective and diffusive terms are written as

$$\left(\frac{\partial u^2}{\partial x}\right)_{i,j} \approx \frac{1}{\Delta x}\left[\left(\frac{u_{i,j}+u_{i+1,j}}{2}\right)^2 - \left(\frac{u_{i-1,j}+u_{i,j}}{2}\right)^2\right], \tag{12}$$

$$\left(\frac{\partial uv}{\partial y}\right)_{i,j} \approx \frac{1}{\Delta y}\left[\left(\frac{u_{i,j}+u_{i,j+1}}{2}\right)\left(\frac{v_{i,j}+v_{i+1,j}}{2}\right) - \left(\frac{u_{i,j-1}+u_{i,j}}{2}\right)\left(\frac{v_{i,j-1}+v_{i+1,j-1}}{2}\right)\right], \tag{13}$$

$$\left(\frac{\partial p}{\partial x}\right)_{i,j} \approx \frac{p_{i,j}-p_{i-1,j}}{\Delta x}, \tag{14}$$

$$\left(\frac{\partial^2 u}{\partial x^2}\right)_{i,j} \approx \frac{u_{i+1,j}-2u_{i,j}+u_{i-1,j}}{\Delta x^2}, \tag{15}$$

$$\left(\frac{\partial^2 u}{\partial y^2}\right)_{i,j} \approx \frac{u_{i,j+1}-2u_{i,j}+u_{i,j-1}}{\Delta y^2}. \tag{16}$$

Defining the convective contribution as

$$C_u = \left(\frac{\partial u^2}{\partial x}\right)_{i,j} + \left(\frac{\partial uv}{\partial y}\right)_{i,j},$$

the pressure-gradient term as

$$P_u = \left(\frac{\partial p}{\partial x}\right)_{i,j},$$

and the viscous contribution as

$$D_u = \frac{1}{Re}\left[\left(\frac{\partial^2 u}{\partial x^2}\right)_{i,j} + \left(\frac{\partial^2 u}{\partial y^2}\right)_{i,j}\right],$$

the explicit u-update becomes

$$u_{i,j}^{n+1} = u_{i,j}^{n} - \Delta\tau\left(C_u + P_u - D_u\right). \tag{17}$$

4.3 Discrete y-momentum equation

For the vertical velocity component, Eq. (3) is discretized as

$$\frac{v_{i,j}^{n+1}-v_{i,j}^{n}}{\Delta\tau} + \left(\frac{\partial uv}{\partial x}\right)_{i,j}^{n} + \left(\frac{\partial v^2}{\partial y}\right)_{i,j}^{n} = -\left(\frac{\partial p}{\partial y}\right)_{i,j}^{n} + \frac{1}{Re}\left[\left(\frac{\partial^2 v}{\partial x^2}\right)_{i,j}^{n} + \left(\frac{\partial^2 v}{\partial y^2}\right)_{i,j}^{n}\right]. \tag{18}$$

The discrete terms are approximated by

$$\left(\frac{\partial uv}{\partial x}\right)_{i,j} \approx \frac{1}{\Delta x}\left[\left(\frac{u_{i,j}+u_{i,j+1}}{2}\right)\left(\frac{v_{i,j}+v_{i+1,j}}{2}\right) - \left(\frac{u_{i-1,j}+u_{i-1,j+1}}{2}\right)\left(\frac{v_{i-1,j}+v_{i,j}}{2}\right)\right], \tag{19}$$

$$\left(\frac{\partial v^2}{\partial y}\right)_{i,j} \approx \frac{1}{\Delta y}\left[\left(\frac{v_{i,j}+v_{i,j+1}}{2}\right)^2 - \left(\frac{v_{i,j-1}+v_{i,j}}{2}\right)^2\right], \tag{20}$$

$$\left(\frac{\partial p}{\partial y}\right)_{i,j} \approx \frac{p_{i,j}-p_{i,j-1}}{\Delta y}, \tag{21}$$

$$\left(\frac{\partial^2 v}{\partial x^2}\right)_{i,j} \approx \frac{v_{i+1,j}-2v_{i,j}+v_{i-1,j}}{\Delta x^2}, \tag{22}$$

$$\left(\frac{\partial^2 v}{\partial y^2}\right)_{i,j} \approx \frac{v_{i,j+1}-2v_{i,j}+v_{i,j-1}}{\Delta y^2}. \tag{23}$$

With

$$C_v = \left(\frac{\partial uv}{\partial x}\right)_{i,j} + \left(\frac{\partial v^2}{\partial y}\right)_{i,j}, \qquad P_v = \left(\frac{\partial p}{\partial y}\right)_{i,j}, \qquad D_v = \frac{1}{Re}\left[\left(\frac{\partial^2 v}{\partial x^2}\right)_{i,j} + \left(\frac{\partial^2 v}{\partial y^2}\right)_{i,j}\right],$$

the explicit v-update is

$$v_{i,j}^{n+1} = v_{i,j}^{n} - \Delta\tau\left(C_v + P_v - D_v\right). \tag{24}$$

5 Boundary Conditions

The physical boundary conditions for the lid-driven cavity are

$$u(x,1) = U_{\text{lid}} = 1, \qquad v(x,1) = 0 \qquad \text{(top moving lid)}, \tag{25}$$

$$u(x,0) = 0, \qquad v(x,0) = 0 \qquad \text{(bottom wall)}, \tag{26}$$

$$u(0,y) = 0, \qquad v(0,y) = 0 \qquad \text{(left wall)}, \tag{27}$$

$$u(1,y) = 0, \qquad v(1,y) = 0 \qquad \text{(right wall)}. \tag{28}$$

For the staggered-grid implementation, these conditions are enforced using ghost-cell relations. A standard second-order treatment is

$$u_{i,0} = -u_{i,1}, \qquad v_{i,0} = 0 \qquad \text{(bottom wall)}, \tag{29}$$

$$u_{i,N+1} = 2U_{\text{lid}} - u_{i,N}, \qquad v_{i,N+1} = 0 \qquad \text{(top wall)}, \tag{30}$$

$$u_{0,j} = 0, \qquad v_{0,j} = -v_{1,j} \qquad \text{(left wall)}, \tag{31}$$

$$u_{N+1,j} = 0, \qquad v_{N+1,j} = -v_{N,j} \qquad \text{(right wall)}. \tag{32}$$

6 Stability and Choice of Timestep

The explicit formulation is limited by a pseudo-acoustic stability condition and by the convective CFL constraint. Since the artificial compressibility method introduces a pseudo-wave speed

$$\hat{c} = \frac{1}{\sqrt{\beta}}, \tag{33}$$

a stability condition for the explicit update is

$$\frac{\hat{c}\,\Delta\tau}{\Delta x} < 1 \qquad \Longrightarrow \qquad \Delta\tau < \Delta x\sqrt{\beta}. \tag{34}$$

A convective CFL condition also gives

$$U\,\Delta\tau < \Delta x. \tag{35}$$

In practice, several timesteps were tested and a stable value was selected for each grid. The values documented are listed in Table 2.

Table 2: Grid sizes and selected pseudo-timesteps used in the simulations.

Grid size N	21	41	61	101
Δx	0.05	0.025	0.0167	0.01
$\Delta\tau_{\text{max}}$ from Eq. (34)	0.035	0.018	0.012	0.007
Selected $\Delta\tau$ for $Re = 100$	0.0025	0.0025	0.0025	0.001
Selected $\Delta\tau$ for $Re = 400$	0.002	0.001	0.001	0.001

The explicit method therefore remains straightforward to implement, but it requires relatively small pseudo-timesteps for stability, especially as the grid is refined and the Reynolds number increases.

7 Solution Procedure

The numerical algorithm used for each case can be summarized as follows:

1. Initialize u, v, and p over the staggered grid.
2. Apply boundary conditions at all walls.
3. Advance the horizontal velocity field using Eq. (17).
4. Advance the vertical velocity field using Eq. (24).
5. Update pressure using Eq. (10).
6. Evaluate the continuity residual,

$$\mathcal{R} = \sum_{i,j} \left| \frac{u_{i,j} - u_{i-1,j}}{\Delta x} + \frac{v_{i,j} - v_{i,j-1}}{\Delta y} \right|. \tag{36}$$

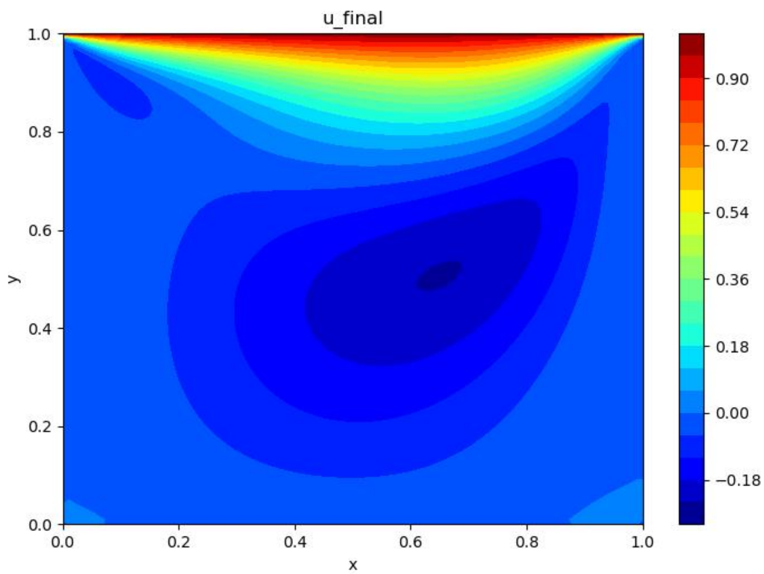

Figure 3: Plot of the horizontal velocity (u) for $Re = 100$.

7. Repeat until $\mathcal{R} < 10^{-4}$.

After convergence, the staggered velocity components are interpolated to a collocated representation for post-processing, plotting, and comparison against benchmark centerline data.

8 Results and Discussion

8.1 Case I: Reynolds number $Re = 100$

For $Re = 100$, the flow remains laminar and strongly influenced by viscous diffusion. The horizontal velocity is largest near the moving lid and decreases progressively toward the bottom wall. The velocity contours are smooth and nearly symmetric, reflecting the relatively mild inertial effects at this Reynolds number.

A primary recirculating vortex forms near the center of the cavity. The u-velocity contours indicate the development of boundary layers near the moving lid and the side walls, where the velocity gradients are steepest. The vertical velocity field exhibits the expected upward and downward motion associated with the cavity recirculation, with stronger redirection of flow near the walls and corners.

The continuity residual decreases monotonically with iteration and reaches the prescribed tolerance after roughly 4.5×10^4 iterations. This relatively large iteration count is a direct consequence of the explicit pseudo-time stepping strategy and the conservative timestep required for stability.

Centerline profiles of u along the vertical midline and v along the horizontal midline were compared with the benchmark data of Ghia et al. The numerical solution follows the benchmark trends

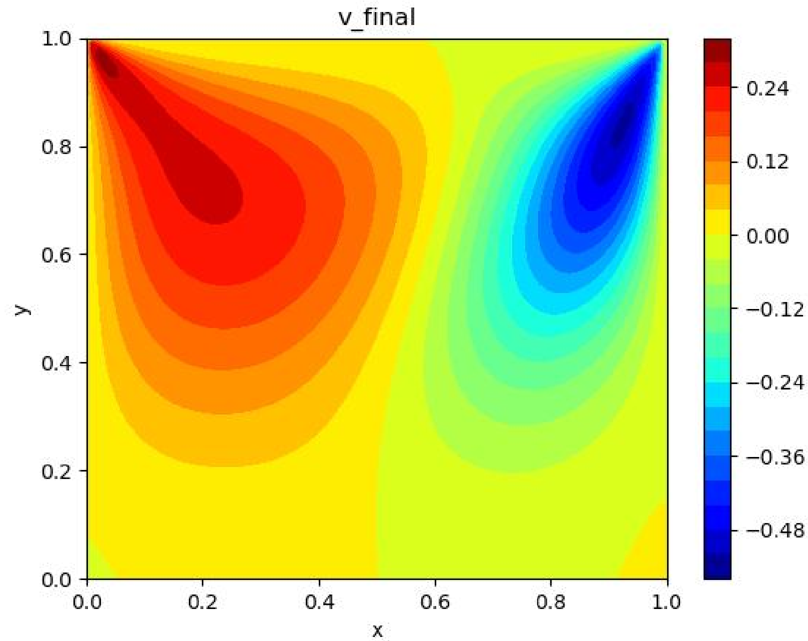

Figure 4: Plot of vertical component of velocity (v) for $Re = 100$.

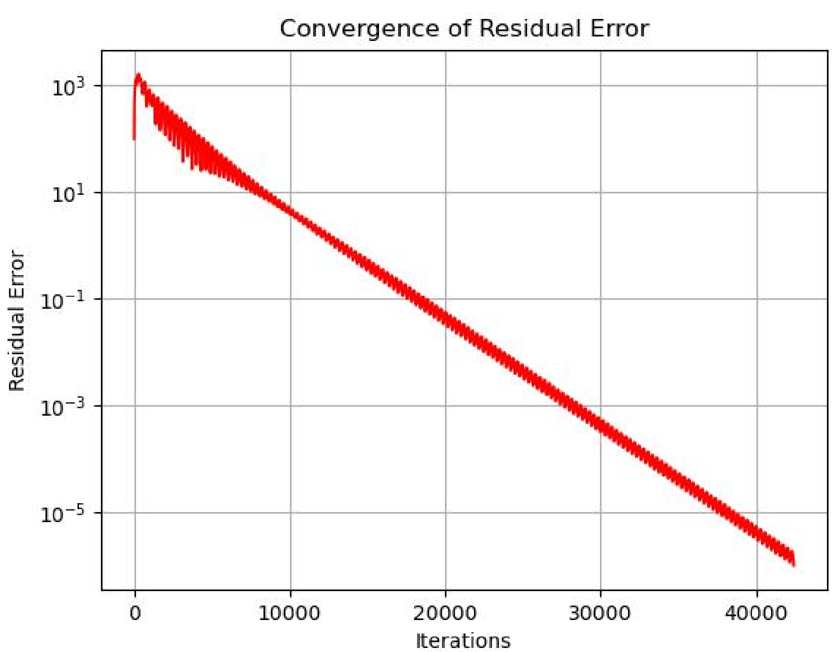

Figure 5: Plot of residual error with iterations for $Re = 100$.

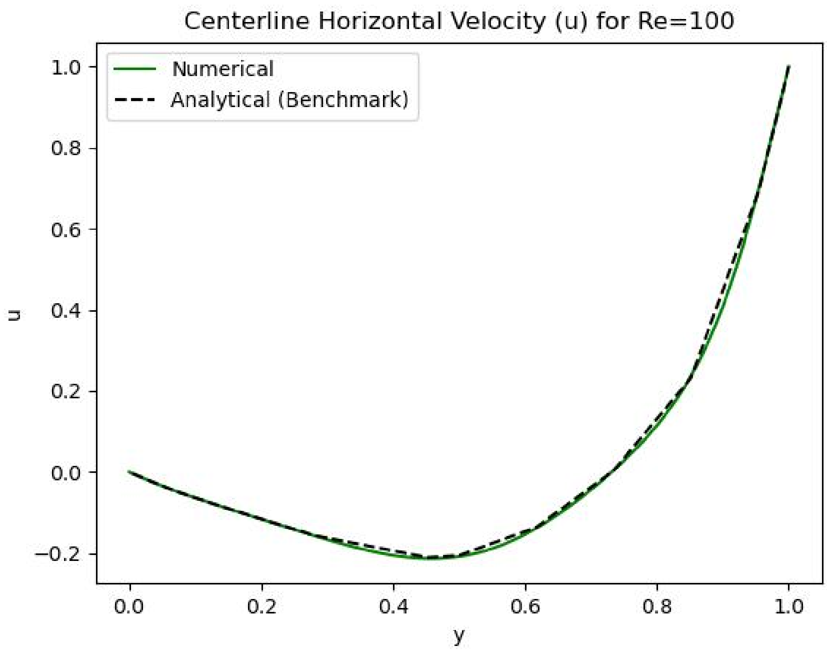

Figure 6: Centerline horizontal velocity (u) for $Re = 100$.

closely, indicating that the artificial compressibility formulation and the staggered-grid discretization accurately capture the main features of the cavity flow at this Reynolds number.

The streamline field confirms the presence of a dominant central vortex, while the contour representation of u suggests the onset of weak corner recirculation zones that remain comparatively small at $Re = 100$.

8.2 Case II: Reynolds number $Re = 400$

At $Re = 400$, inertial effects are more significant and the flow becomes noticeably more asymmetric. The primary vortex remains the dominant structure in the cavity, but it is more elongated and displaced relative to the $Re = 100$ case. Stronger velocity gradients appear near the moving lid and in the corner regions, indicating thinner boundary layers and more pronounced recirculating motion.

The vertical velocity field shows sharper gradients and a larger magnitude near the upper corners, while the horizontal velocity contour reveals a deeper penetration of lid-induced motion into the cavity interior. These trends are consistent with the increase in Reynolds number and the reduced relative influence of viscosity.

The residual history shows stronger oscillatory behavior during the transient convergence process and requires approximately 1.6×10^5 iterations to reach the convergence tolerance. Compared with the $Re = 100$ case, the higher Reynolds number produces larger local fluctuations in the explicit pseudo-time iterations and substantially increases the number of iterations required to reach steady state.

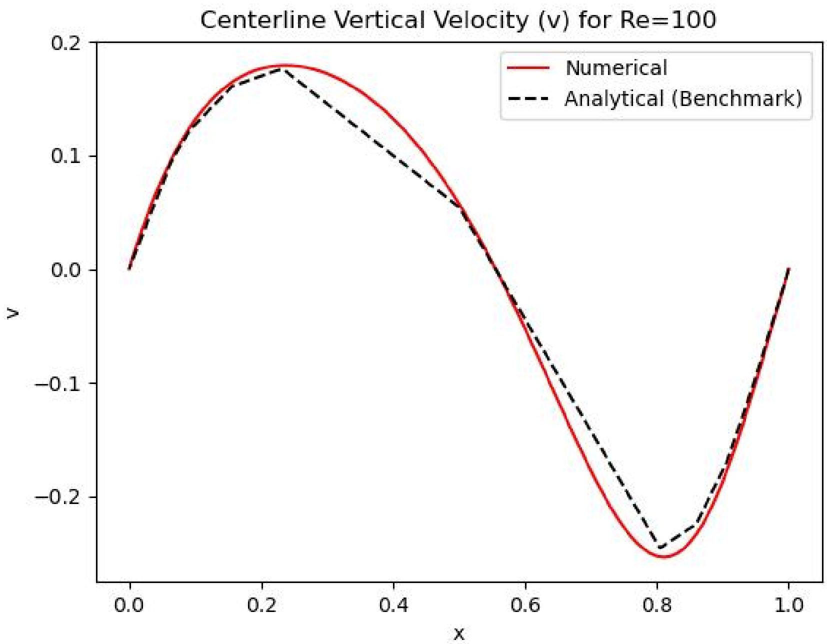

Figure 7: Centerline vertical velocity (v) for $Re = 100$.

TABLE I

Results for *u*-velocity along Vertical Line through Geometric Center of Cavity

129-grid pt. no.	*y*	Re						
		100	400	1000	3200	5000	7500	10,000
129	1.00000	1.00000	1.00000	1.00000	1.00000	1.00000	1.00000	1.00000
126	0.9766	0.84123	0.75837	0.65928	0.53236	0.48223	0.47244	0.47221
125	0.9688	0.78871	0.68439	0.57492	0.48296	0.46120	0.47048	0.47783
124	0.9609	0.73722	0.61756	0.51117	0.46547	0.45992	0.47323	0.48070
123	0.9531	0.68717	0.55892	0.46604	0.46101	0.46036	0.47167	0.47804
110	0.8516	0.23151	0.29093	0.33304	0.34682	0.33556	0.34228	0.34635
95	0.7344	0.00332	0.16256	0.18719	0.19791	0.20087	0.20591	0.20673
80	0.6172	−0.13641	0.02135	0.05702	0.07156	0.08183	0.08342	0.08344
65	0.5000	−0.20581	−0.11477	−0.06080	−0.04272	−0.03039	−0.03800	0.03111
59	0.4531	−0.21090	−0.17119	−0.10648	−0.86636	−0.07404	−0.07503	−0.07540
37	0.2813	−0.15662	−0.32726	−0.27805	−0.24427	−0.22855	−0.23176	−0.23186
23	0.1719	−0.10150	−0.24299	−0.38289	−0.34323	−0.33050	−0.32393	−0.32709
14	0.1016	−0.06434	−0.14612	−0.29730	−0.41933	−0.40435	−0.38324	−0.38000
10	0.0703	−0.04775	−0.10338	−0.22220	−0.37827	−0.43643	−0.43025	−0.41657
9	0.0625	−0.04192	−0.09266	−0.20196	−0.35344	−0.42901	−0.43590	−0.42537
8	0.0547	−0.03717	−0.08186	−0.18109	−0.32407	−0.41165	−0.43154	−0.42735
1	0.0000	0.00000	0.00000	0.00000	0.00000	0.00000	0.00000	0.00000

Figure 8: Data for centerline horizontal velocity from Ghia et al.

TABLE II

Results for v-Velocity along Horizontal Line through Geometric Center of Cavity

129-grid pt. no.	x	Re 100	400	1000	3200	5000	7500	10,000
129	1.0000	0.00000	0.00000	0.00000	0.00000	0.00000	0.00000	0.00000
125	0.9688	−0.05906	−0.12146	−0.21388	−0.39017	−0.49774	−0.53858	−0.54302
124	0.9609	−0.07391	−0.15663	−0.27669	−0.47425	−0.55069	−0.55216	−0.52987
123	0.9531	−0.08864	−0.19254	−0.33714	−0.52357	−0.55408	−0.52347	−0.49099
122	0.9453	−0.10313	−0.22847	−0.39188	−0.54053	−0.52876	−0.48590	−0.45863
117	0.9063	−0.16914	−0.23827	−0.51550	−0.44307	−0.41442	−0.41050	−0.41496
111	0.8594	−0.22445	−0.44993	−0.42665	−0.37401	−0.36214	−0.36213	−0.36737
104	0.8047	−0.24533	−0.38598	−0.31966	−0.31184	−0.30018	−0.30448	−0.30719
65	0.5000	0.05454	0.05186	0.02526	0.00999	0.00945	0.00824	0.00831
31	0.2344	0.17527	0.30174	0.32235	0.28188	0.27280	0.27348	0.27224
30	0.2266	0.17507	0.30203	0.33075	0.29030	0.28066	0.28117	0.28003
21	0.1563	0.16077	0.28124	0.37095	0.37119	0.35368	0.35060	0.35070
13	0.0938	0.12317	0.22965	0.32627	0.42768	0.42951	0.41824	0.41487
11	0.0781	0.10890	0.20920	0.30353	0.41906	0.43648	0.43564	0.43124
10	0.0703	0.10091	0.19713	0.29012	0.40917	0.43329	0.44030	0.43733
9	0.0625	0.09233	0.18360	0.27485	0.39560	0.42447	0.43979	0.43983
1	0.0000	0.00000	0.00000	0.00000	0.00000	0.00000	0.00000	0.00000

Figure 9: Data for centerline vertical velocity from Ghia et al.

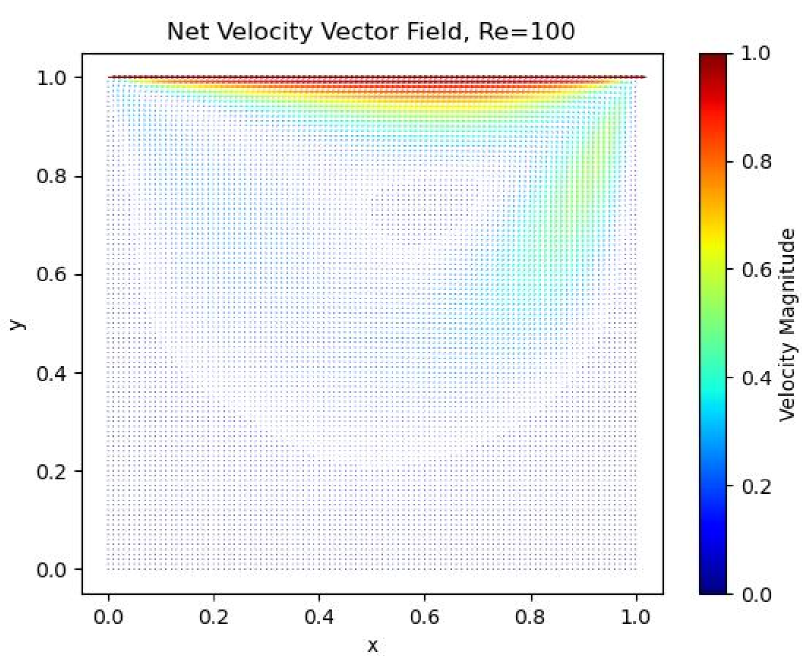

Figure 10: Streamline plot of net velocity vector for $Re = 100$.

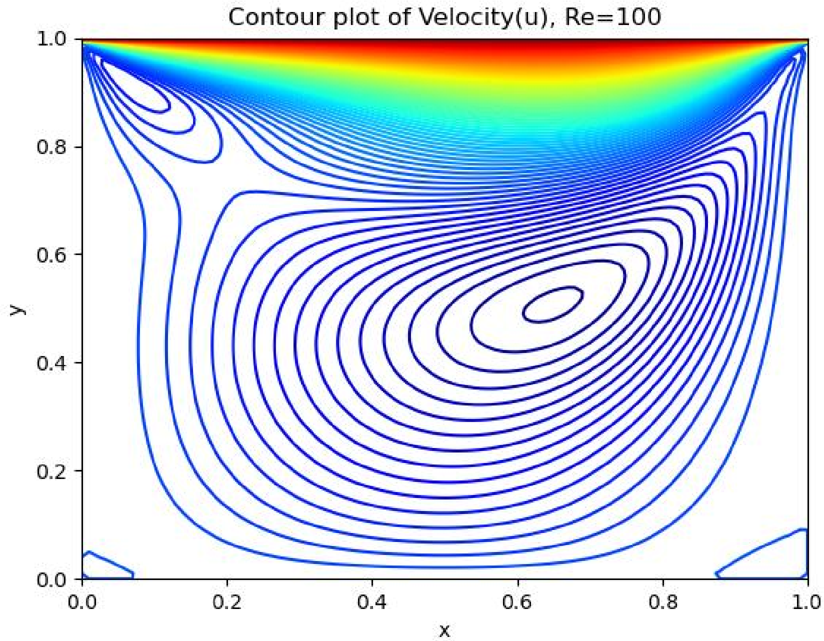

Figure 11: Contour plot of horizontal velocity (u) for $Re = 100$.

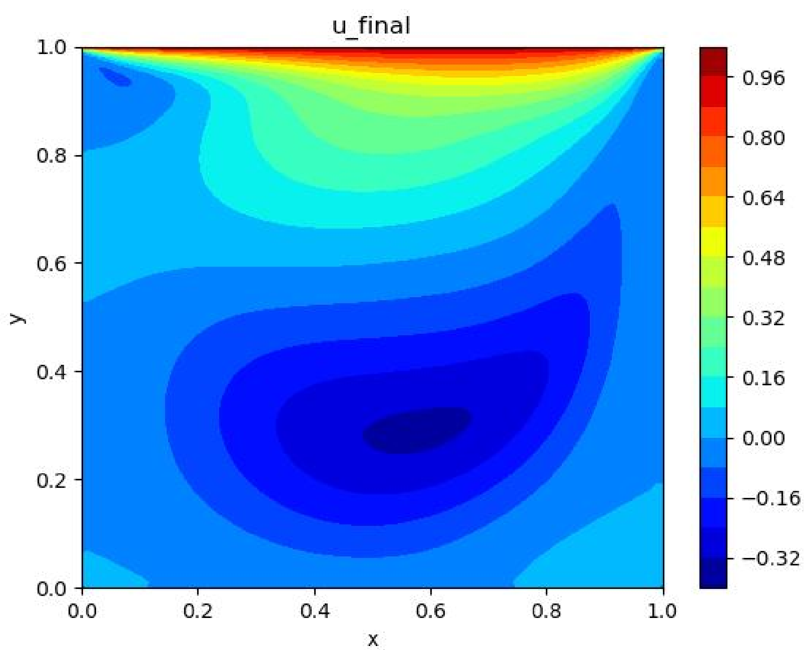

Figure 12: Plot of the horizontal velocity (u) for $Re = 400$.

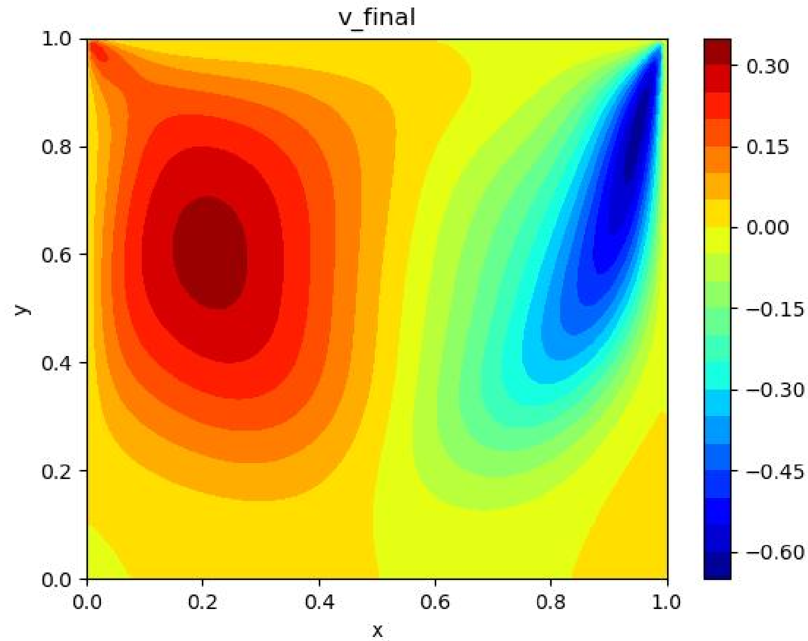

Figure 13: Plot of vertical component of velocity (v) for $Re = 400$.

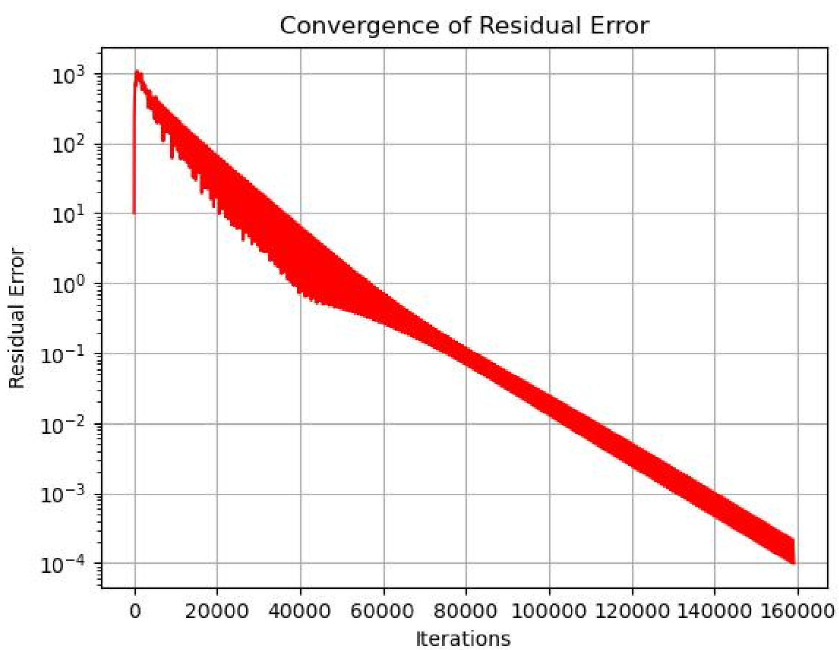

Figure 14: Plot of residual error with iterations for $Re = 400$.

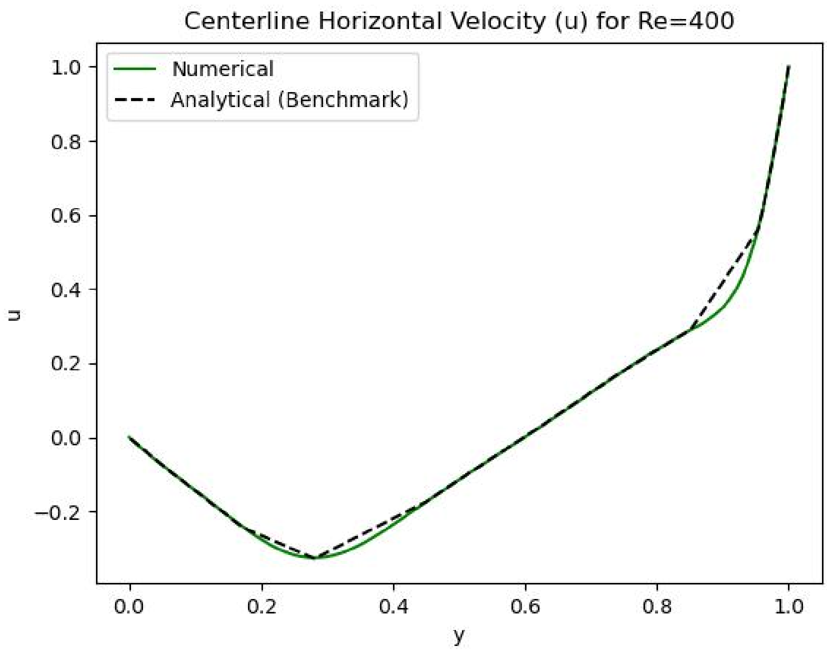

Figure 15: Centerline horizontal velocity (u) for $Re = 400$.

The computed centerline velocity profiles again compare well with the Ghia et al. benchmark data. The agreement remains close, especially in the primary-vortex region, although the higher-Reynolds-number case is naturally more sensitive to grid resolution and timestep selection. Streamlines and u-velocity contours both indicate stronger secondary flow structures near the corners than in the $Re = 100$ case.

8.3 Effect of Reynolds Number

The two cases clearly illustrate the changing balance between viscous and inertial effects in the lid-driven cavity problem.

At $Re = 100$, the solution is smoother and more diffusion-dominated. The central vortex is well defined but relatively rounded, and the propagation of lid-induced momentum into the lower part of the cavity is limited. Secondary vortices are weak or only incipient.

At $Re = 400$, the interior recirculation is stronger and more distorted, the boundary layers are thinner, and corner vortices become more prominent. The effect of the lid penetrates further into the cavity, and the stronger local gradients lead to more oscillatory convergence behavior in the explicit artificial-compressibility iterations.

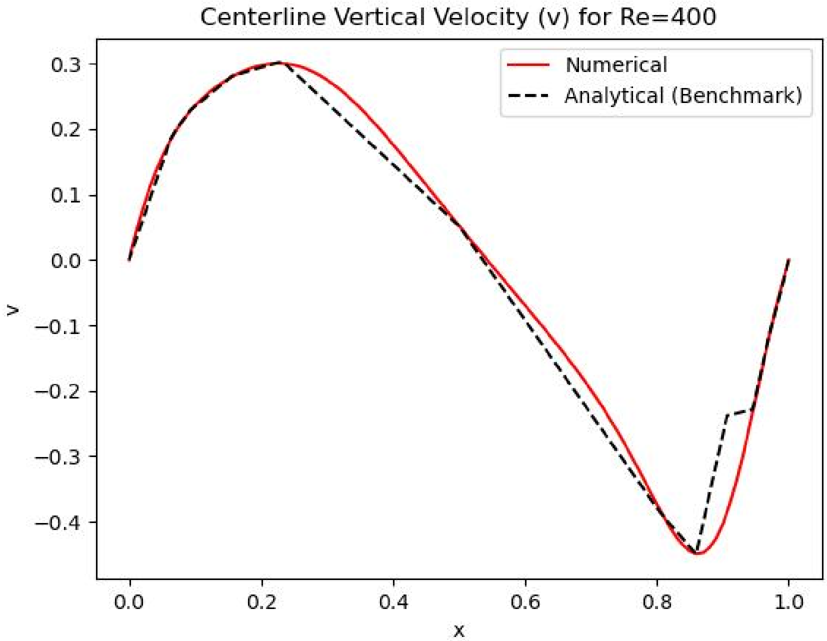

Figure 16: Centerline vertical velocity (v) for $Re = 400$.

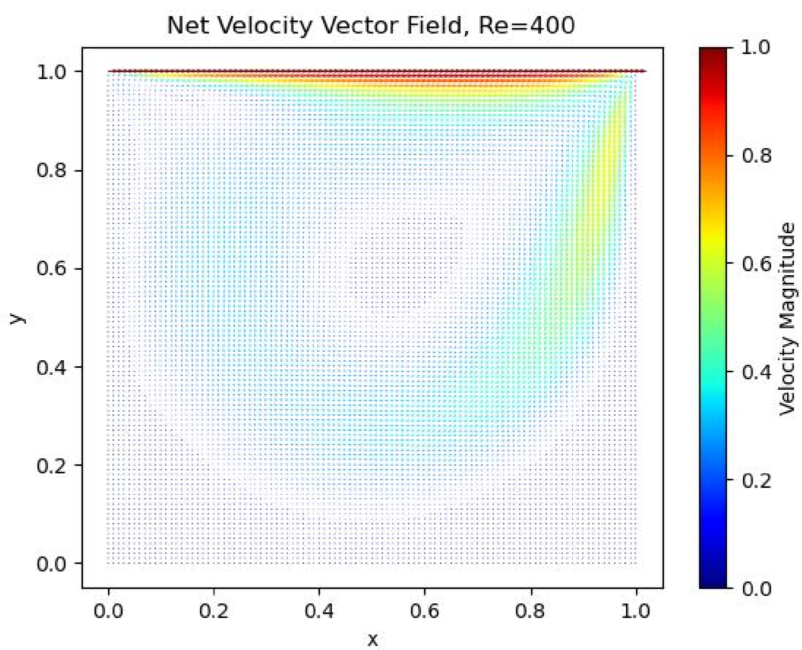

Figure 17: Streamline plot of net velocity vector for $Re = 400$.

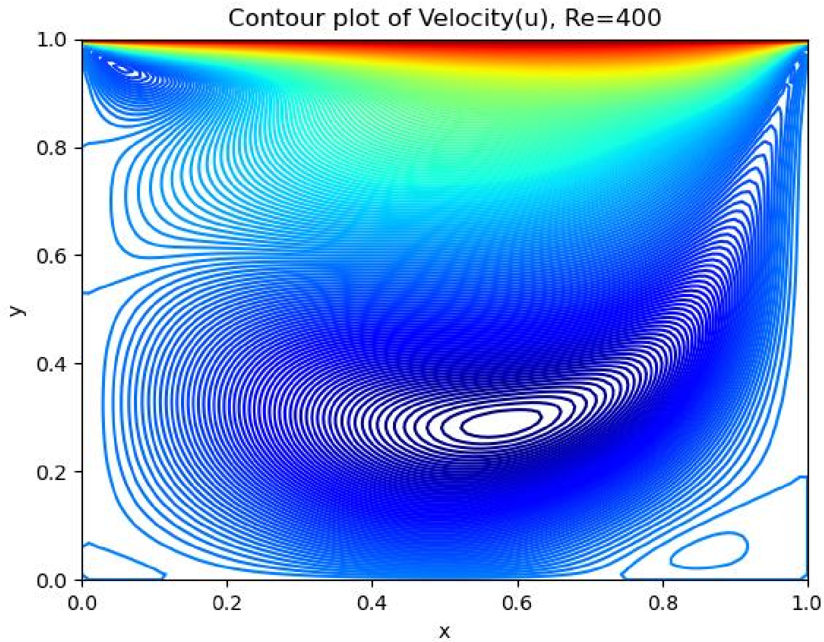

Figure 18: Contour plot of horizontal velocity (u) for $Re = 400$.

9 Validation Against Benchmark Data

To assess solution accuracy, the centerline horizontal velocity $u(y)$ along the vertical geometric centerline and the centerline vertical velocity $v(x)$ along the horizontal geometric centerline were compared with the benchmark data reported by Ghia, Ghia, and Shin. For both Reynolds numbers considered here, the numerical profiles follow the benchmark trends closely.

The agreement is particularly good for $Re = 100$, where the flow is smoother and easier to resolve on moderate grids. For $Re = 400$, the solution still matches the reference data well, but the sharper gradients and stronger corner effects make the comparison more sensitive to grid resolution. Overall, the comparisons support the conclusion that the present staggered-grid artificial-compressibility implementation provides accurate predictions for the lid-driven cavity benchmark.

10 Grid-Convergence Assessment

A spatial convergence study was carried out using three grid sizes, $N = 21$, 41, and 81, and the finest available solution ($N = 101$) was used as the reference for error comparison. The centerline velocity profiles show consistent improvement with grid refinement for both Reynolds numbers.

For $Re = 100$, the refined-grid solutions produce progressively smoother centerline profiles and approach the benchmark data more closely. The same trend is observed for $Re = 400$, although the higher-Reynolds-number solution displays a stronger dependence on grid resolution because of the thinner boundary layers and increased secondary-motion intensity.

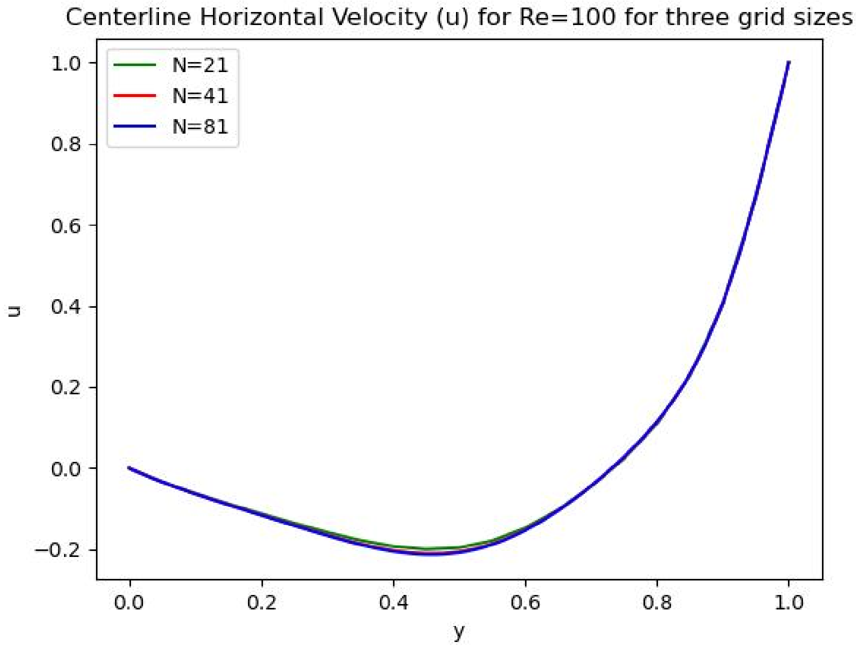

Figure 19: Centerline horizontal velocity for three grid sizes ($N = 21, 41, 81$) for $Re = 100$.

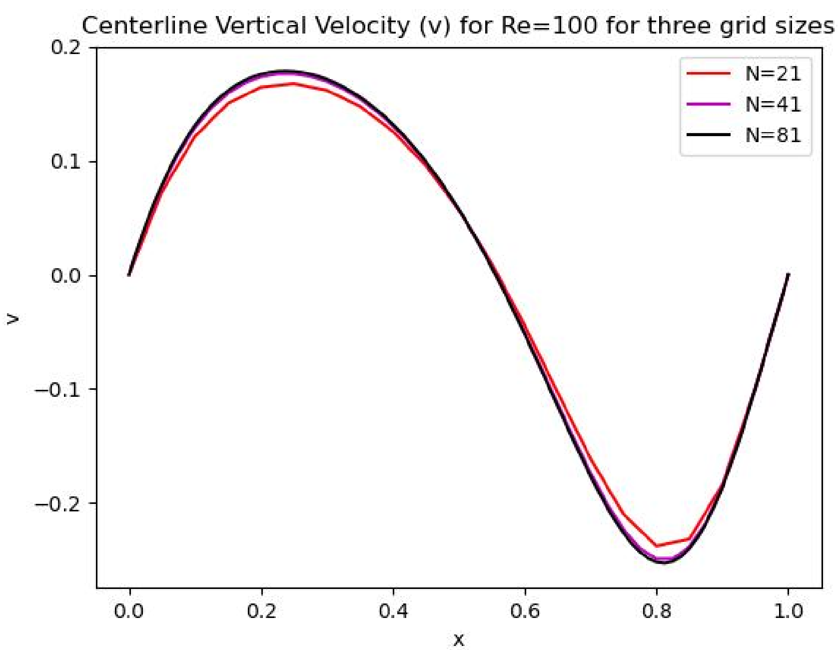

Figure 20: Centerline vertical velocity for three grid sizes ($N = 21, 41, 81$) for $Re = 100$.

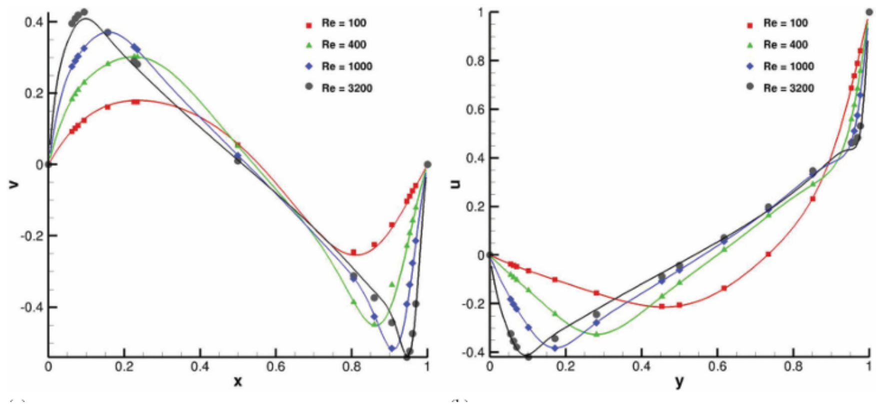

Figure 21: Centerline velocities for the lid-driven cavity: (a) vertical velocity variation and (b) horizontal velocity variation, results from Ghia et al. (1982).

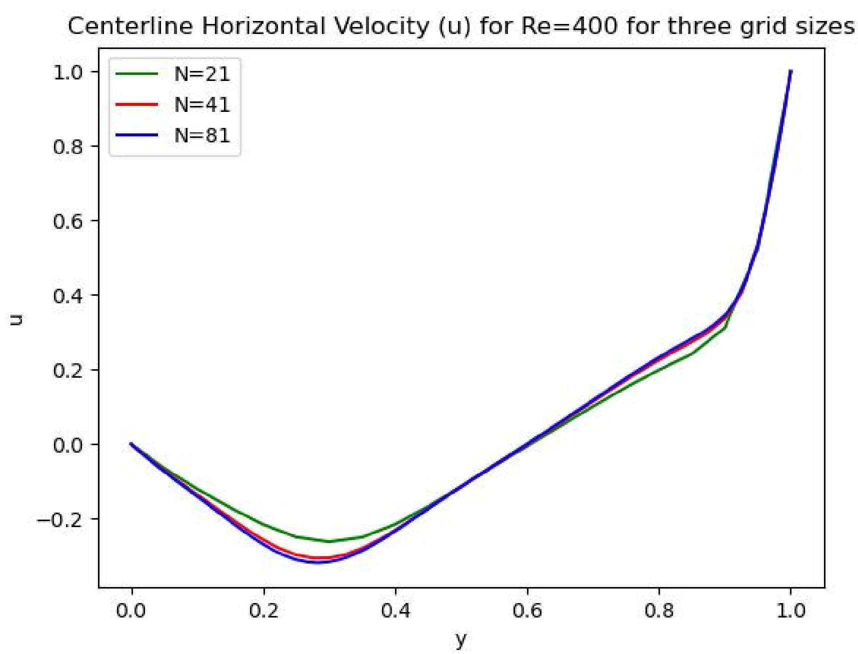

Figure 22: Centerline horizontal velocity for three grid sizes ($N = 21, 41, 81$) for $Re = 400$.

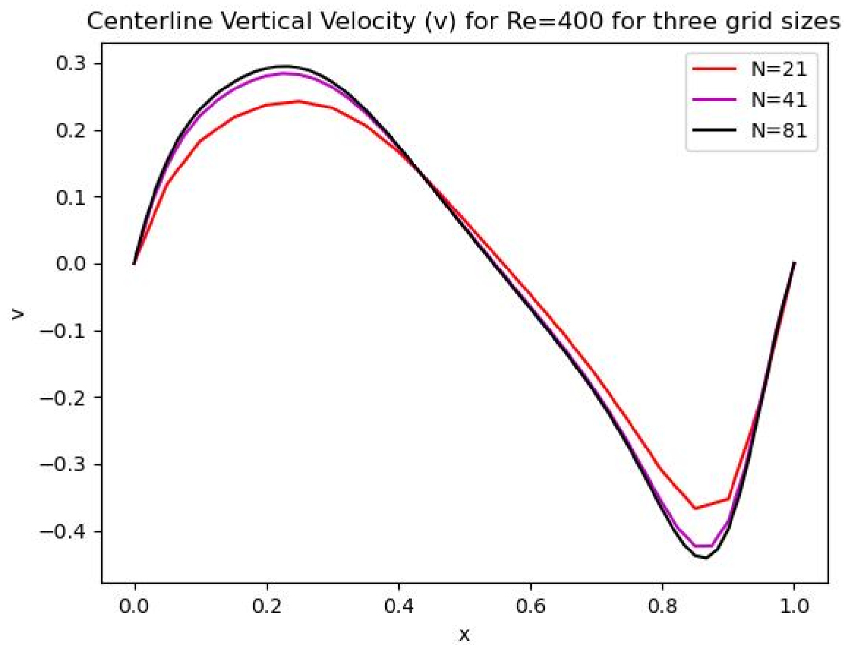

Figure 23: Centerline vertical velocity for three grid sizes ($N = 21, 41, 81$) for $Re = 400$.

The residual histories for the three grids show that finer grids require more iterations to converge because the number of unknowns increases and the stable explicit timestep becomes more restrictive. Nevertheless, the error norm decreases monotonically as the grid is refined, and the observed behavior is consistent with second-order spatial accuracy of the central-difference discretization.

11 Conclusions

A two-dimensional staggered-grid artificial-compressibility solver was used to simulate lid-driven cavity flow at $Re = 100$ and $Re = 400$. The incompressible continuity equation was replaced by a pseudo-time pressure evolution equation, and an explicit update strategy was employed for both pressure and momentum.

The method successfully captured the key physical features of the cavity flow in both cases, including the central vortex, the progressive strengthening of corner recirculation with increasing Reynolds number, and the expected changes in boundary-layer thickness and centerline velocity distributions. Comparison with the benchmark data of Ghia et al. showed good overall agreement, and the grid-convergence study indicated monotonic reduction of error with mesh refinement and behavior consistent with second-order accuracy.

The main limitation of the present implementation is the cost of explicit pseudo-time marching, which demands small timesteps and therefore a large number of iterations, especially for higher Reynolds numbers and finer grids. Even so, the method remains a useful and conceptually clear framework for solving incompressible flows and for validating pressure–velocity coupling on staggered grids.

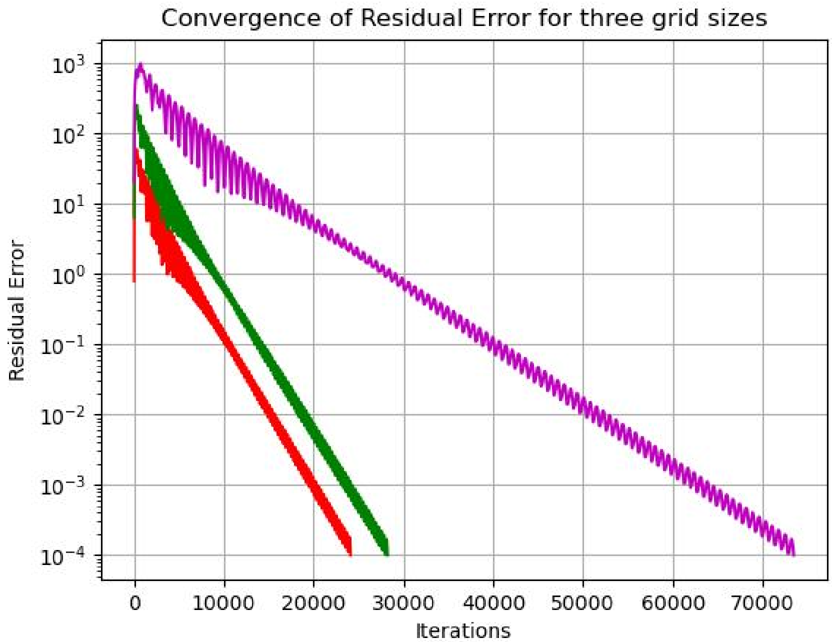

Figure 24: Plot of variation of residual with iterations for $N = 21$ (red), $N = 41$ (green), and $N = 81$ (magenta) for $Re = 100$.

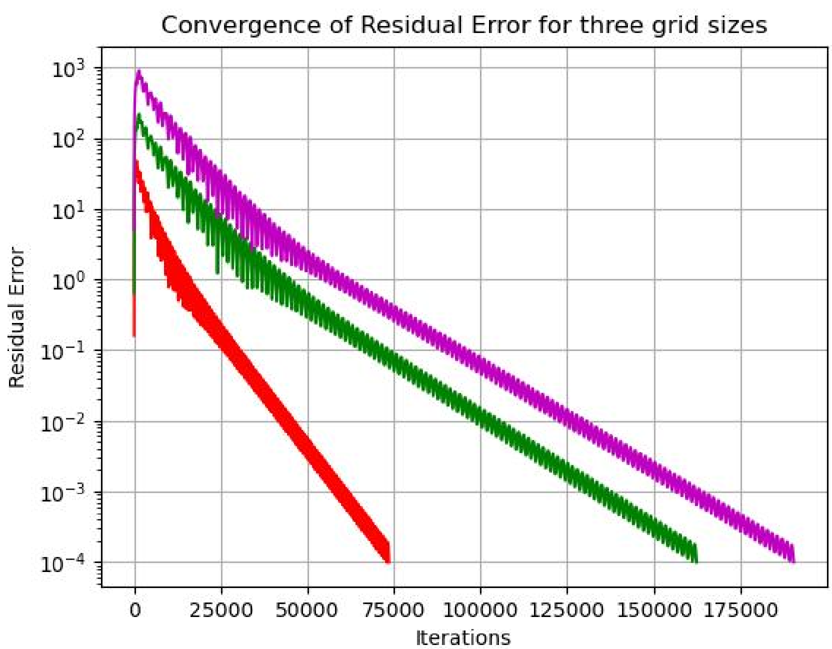

Figure 25: Plot of variation of residual with iterations for $N = 21$ (red), $N = 41$ (green), and $N = 81$ (magenta) for $Re = 400$.

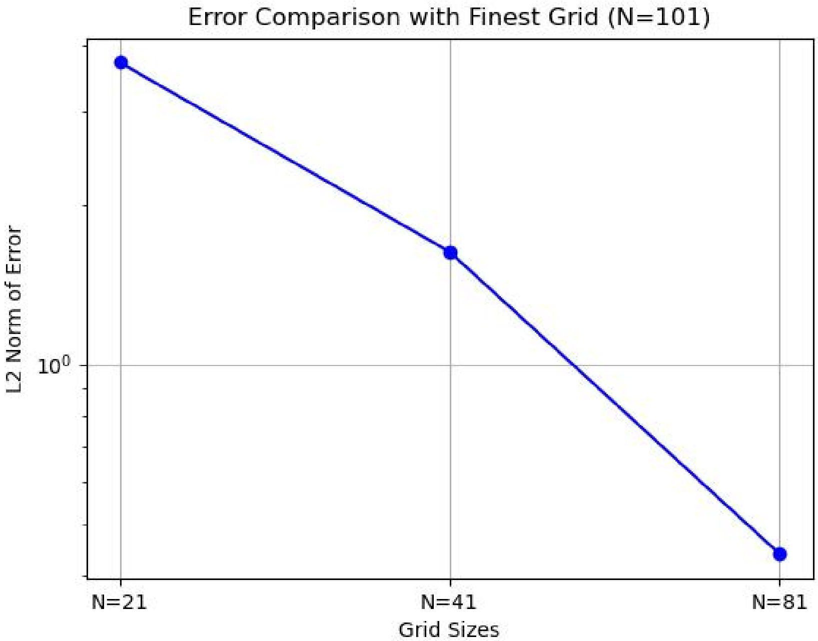

Figure 26: Error comparison with the finest grid ($N = 101$) for $Re = 100$.

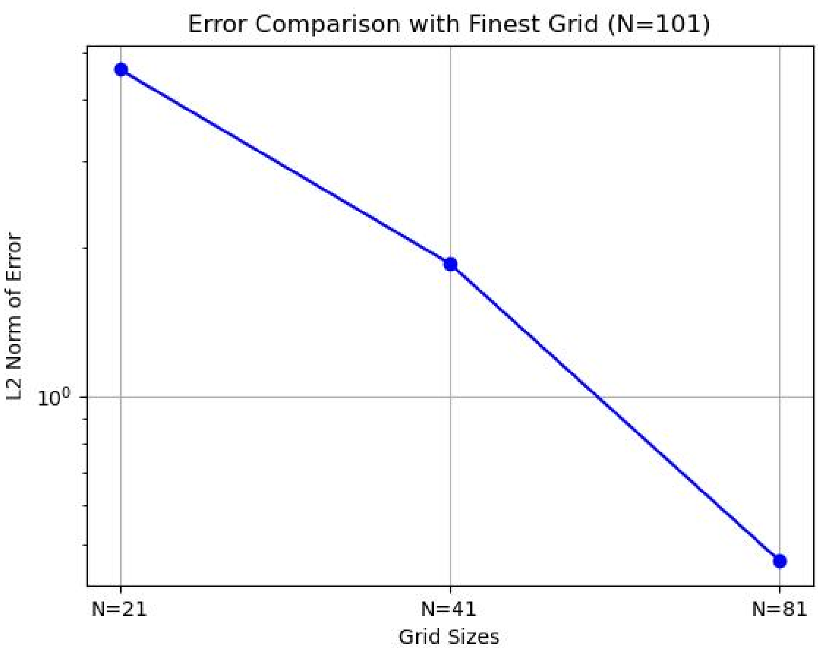

Figure 27: Error comparison with the finest grid ($N = 101$) for $Re = 400$.

References

[1] U. Ghia, K. N. Ghia, and C. T. Shin, "High-Re solutions for incompressible flow using the Navier–Stokes equations and a multigrid method," *Journal of Computational Physics*, vol. 48, no. 3, pp. 387–411, 1982.

[2] A. J. Chorin, "A numerical method for solving incompressible viscous flow problems," *Journal of Computational Physics*, vol. 2, no. 1, pp. 12–26, 1967.

[3] F. H. Harlow and J. E. Welch, "Numerical calculation of time-dependent viscous incompressible flow of fluid with free surface," *Physics of Fluids*, vol. 8, no. 12, pp. 2182–2189, 1965.

[4] P. M. Gresho and R. L. Sani, "On pressure boundary conditions for the incompressible Navier–Stokes equations," *International Journal for Numerical Methods in Fluids*, vol. 7, no. 10, pp. 1111–1145, 1987.

[5] S. E. Rogers and D. Kwak, "An upwind differencing scheme for the incompressible Navier–Stokes equations," *Applied Numerical Mathematics*, vol. 8, no. 1–2, pp. 43–64, 1991.

[6] J. D. Ramshaw and V. A. Mousseau, "Accelerated artificial compressibility method for steady-state incompressible flow calculations," *Computers & Fluids*, vol. 18, no. 4, pp. 361–367, 1990.

[7] P. A. Madsen and H. A. Schäffer, "A discussion of artificial compressibility," *Coastal Engineering*, vol. 53, no. 1, pp. 93–98, 2006.